Chem

CellPress

Article

# Size-Tunable Assemblies Based on Ferrocene-Containing DNA Polymers for Spatially Uniform Penetration

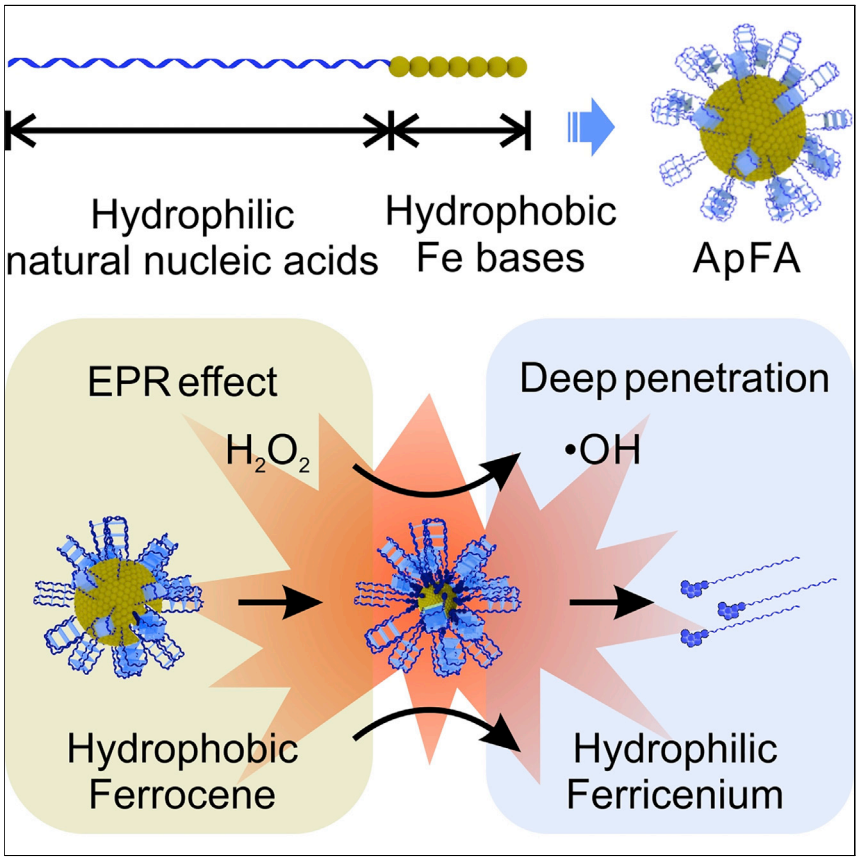


Polymeric micelles have received increased attention in the field of pharmaceutical exploitation. However, supra-100-nm micelles, suitable for the EPR effect, cannot penetrate through the dense collagen matrix in solid tumor tissues, thus decreasing the efficacy of anticancer agents. In this work, amphiphilic nucleic acid polymers with tunable hydrophobicity were designed, and size-tunable nucleic acid assemblies were developed to resolve the conflict between EPR effect and spatially uniform penetration ability.

Jie Tan, Hao Li, Xiaoxiao Hu, ..., Zhijun Sun, Quan Yuan, Weihong Tan

yuanquan@whu.edu.cn (Q.Y.)
tan@chem.ufl.edu (W.T.)

## HIGHLIGHTS

Developing size-tunable DNA micelles showing EPR effect and deep penetration

Controlled assembly of nucleic acid polymers

Producing Fenton-like reaction-performing amphiphilic nucleic acid polymers

This micellar system can be expanded by integrating functional nucleic acids

Tan et al., Chem 5, 1–18
July 11, 2019 © 2019 Published by Elsevier Inc.
https://doi.org/10.1016/j.chempr.2019.05.024

Please cite this article in press as: Tan et al., Size-Tunable Assemblies Based on Ferrocene-Containing DNA Polymers for Spatially Uniform Penetration, Chem (2019), https://doi.org/10.1016/j.chempr.2019.05.024

Chem

CellPress

Article

# Size-Tunable Assemblies Based on Ferrocene-Containing DNA Polymers for Spatially Uniform Penetration

Jie Tan,[1] Hao Li,[3] Xiaoxiao Hu,[1] Razack Abdullah,[1] Sitao Xie,[1] Lili Zhang,[1] Mengmeng Zhao,[1] Qiang Luo,[1] Yazhou Li,[1] Zhijun Sun,[3] Quan Yuan,[1,4,*] and Weihong Tan[1,2,5,*]

## SUMMARY

**Polymeric assemblies in the range of 100 nm can accumulate effectively around tumor tissue via the enhanced permeability and retention (EPR) effect. However, the desirable diameter for spatially uniform penetration is less than 30 nm, conflicting with requirements specified for the EPR effect. Here, a ferrocene-containing nucleic acid polymer was designed, and a size-tunable assembly system was developed to resolve the conflict between the EPR effect and spatially uniform penetration. Specifically, assemblies in the range of 100 nm can accumulate around the tumor via the EPR effect rapidly. After exposure to the tumor microenvironment, ferrocene moieties in this assembly can undergo a Fenton-like reaction that results in remarkable size shrinkage to 10 nm, thereby improving the tumor penetration ability of the assembly. These nucleic acid assemblies can also release highly toxic hydroxyl radicals into the tumor microenvironment, achieving *in vivo* catalytic therapy for efficient cancer treatment.**

## INTRODUCTION

Based on their suitable size, polymeric assemblies have gained increasing attention in the pharmaceutical field.[1–3] Polymeric assemblies can provide a versatile platform for the design of size-controlled pharmaceutics.[4,5] Assemblies in the range of 100 nm can accumulate around the leaky regions of tumor vessels via the EPR effect since vascular permeability around tumor tissue is greater than that of normal tissue.[6–8] Additionally, drugs encapsulated in assemblies can also be sustainably released. With all these advantages, polymeric assemblies hold great potential for effective cancer therapy. However, the dense collagen matrix in tumor tissue could hinder the further penetration and internalization of supra-100-nm drugs to reach the central portion of tumor tissue, thus decreasing the efficacy of anticancer agents.[9–12] On the contrary, assemblies less than 30 nm have improved tumor penetration but suffer from inferior tumor accumulation.[4,9,13,14] As mentioned above, the EPR size requirement is about 100 nm, which conflicts with the tumor-penetrating requirements.

Depending on their chemical structure, amphiphilic polymers can self-assemble into assemblies with different sizes controlled by adjusting the ratio of the hydrophilic/hydrophobic segments.[15–19] Therefore, the rational design of polymer chemical structures to form a size-tunable assembly is a promising strategy to solve the above dilemma.[1,20–23] Considering both the EPR effect and tumor penetration, ideal

### The Bigger Picture

Because of their ability to load therapeutics, deliver the cargo to the tumor via the EPR effect, and sustainably release the loaded drugs, polymeric micelles have received increased attention in the field of pharmaceutical exploitation. However, supra-100-nm micelles, suitable for the EPR effect, cannot penetrate through the dense collagen matrix in solid tumor tissues, thus decreasing the efficacy of anticancer agents. In this work, we designed a size-tunable assembly system able to resolve the conflict between the EPR effect and spatially uniform penetration ability.

This nucleic-acid-based micellar system can be expanded by integrating functional nucleic acids. As a designable and programmable biomolecule, nucleic-acid-based micelles can provide possibilities for blood-brain-barrier penetration and gene transfer.

Please cite this article in press as: Tan et al., Size-Tunable Assemblies Based on Ferrocene-Containing DNA Polymers for Spatially Uniform Penetration, Chem (2019), https://doi.org/10.1016/j.chempr.2019.05.024



assemblies should have two features. First, the initial size of assemblies should around 100 nm to accumulate around tumor tissues via the EPR effect. Second, when arriving at tumor tissues, assemblies must achieve a size reduction to penetrate deeper. As a programmable biomolecule with strong recognition capability and self-assembling properties, nucleic acids can provide possibilities for various modifications.[24,25] By modification, the hydrophobicity of nucleic acids could be changed, and the sizes of nucleic acid assemblies could be regulated.[26,27] Additionally, nucleic acid assemblies can serve as ideal carriers because of their superior biocompatibility.[24,25] Based on these properties, amphiphilic nucleic acid polymers hold great potential to construct size-tunable assemblies to meet the requirements during circulation and penetration.

As a typical Fenton reagent, ferrocene contains two parallel cyclopentadiene rings, which endow ferrocene with strong hydrophobicity.[28] An electron transfer process from the ferrocenyl group to $H_2O_2$ has been proved in a Fenton-like reaction, and the hydrophobic $Fe(Cp)_2$ can be changed into hydrophilic $Fe(Cp)_2^+$ during this reaction.[29–31] In light of this, by using amphiphilic ferrocene-containing nucleic acid polymers as the building blocks, we report the design of a size-tunable aptamer-ferrocene assembly (denoted as ApFA) to resolve the conflict between the EPR effect and deep penetration ability. Ferrocene moieties in ApFAs can undergo a Fenton-like reaction and change their hydrophobicity, resulting in remarkable size shrinkage of ApFAs. Meanwhile, Fe (III) produced by the Fenton reaction can be used as an MRI negative contrast agent to characterize the penetration ability of ApFAs *in vivo*.[32–34] Additionally, as a byproduct of the Fenton reaction, the ApFA system can also release highly toxic hydroxyl radicals able to induce tumor cell death for cancer treatment.[35–39] As a step forward, natural glucose oxidase (GOD) was loaded in ApFAs since GOD can catalyze the reaction of glucose to produce abundant $H_2O_2$. The elevated $H_2O_2$ further participates in ApFA-mediated Fenton-like reaction to liberate large quantities of highly toxic hydroxyl radicals that can significantly enhance the efficiency of tumor apoptosis. The co-delivery of GOD and ApFAs to cancer cells can realize spatially uniform penetration by size shrinkage of ApFAs and provide a tumor therapy by yielding hydroxyl radicals. Overall, these nucleic acid assemblies not only offer a concept for the design of drug delivery systems featuring both an excellent EPR effect and deep tumor penetration but also provide a promising step toward biopharmaceutics for cancer treatment.

## RESULTS

### Characterization of ApFAs

As illustrated in Figure 1A, size-tunable ApFAs were formed by self-assembly of aptamer-$Fe_n$. Hydrophilic nucleic acid segments were positioned on the surface of assemblies as a corona, while the hydrophobic Fe-base segments formed the core of assemblies. The G-rich aptamer S13, which targets A549 cells, was designed as flares to enhance targeting and internalization of ApFAs.[40] Additionally, parallel G-quadruplexes and π-π conjugated ferrocene moieties were introduced into the ApFA system to lock and stabilize the entire structure.[41,42]

The essential size-tunable concept of ApFAs was based on the tumor microenvironment-mediated Fenton-like reaction and the resulting hydrophilic/hydrophobic ratio variation. ApFAs with a large initial size can accumulate around solid tumors via the EPR effect. When in the acidic tumor microenvironment, ferrocene moieties in ApFAs can undergo a Fenton-like reaction and change the

[1]Molecular Science and Biomedicine Laboratory (MBL), Institute of Chemical Biology and Nanomedicine, State Key Laboratory of Chemo/Biosensing and Chemometrics, College of Chemistry and Chemical Engineering, College of Biology, and Aptamer Engineering Center of Hunan Province, Hunan University, Changsha 410082, China

[2]Department of Chemistry and Department of Physiology and Functional Genomics, Center for Research at the Bio/Nano Interface, Health Cancer Center, UF Genetics Institute and McKnight Brain Institute, University of Florida, Gainesville, FL 32611-7200, USA

[3]State Key Laboratory Breeding Base of Basic Science of Stomatology (Hubei-MOST) & Key Laboratory of Oral Bio-medicine Ministry of Education, School & Hospital of Stomatology, Wuhan University, Wuhan 430072, China

[4]Key Laboratory of Analytical Chemistry for Biology and Medicine (Ministry of Education), College of Chemistry and Molecular Sciences, Wuhan University, Wuhan 430072, China

[5]Lead Contact

*Correspondence: yuanquan@whu.edu.cn (Q.Y.), tan@chem.ufl.edu (W.T.)

https://doi.org/10.1016/j.chempr.2019.05.024

Please cite this article in press as: Tan et al., Size-Tunable Assemblies Based on Ferrocene-Containing DNA Polymers for Spatially Uniform Penetration, Chem (2019), https://doi.org/10.1016/j.chempr.2019.05.024



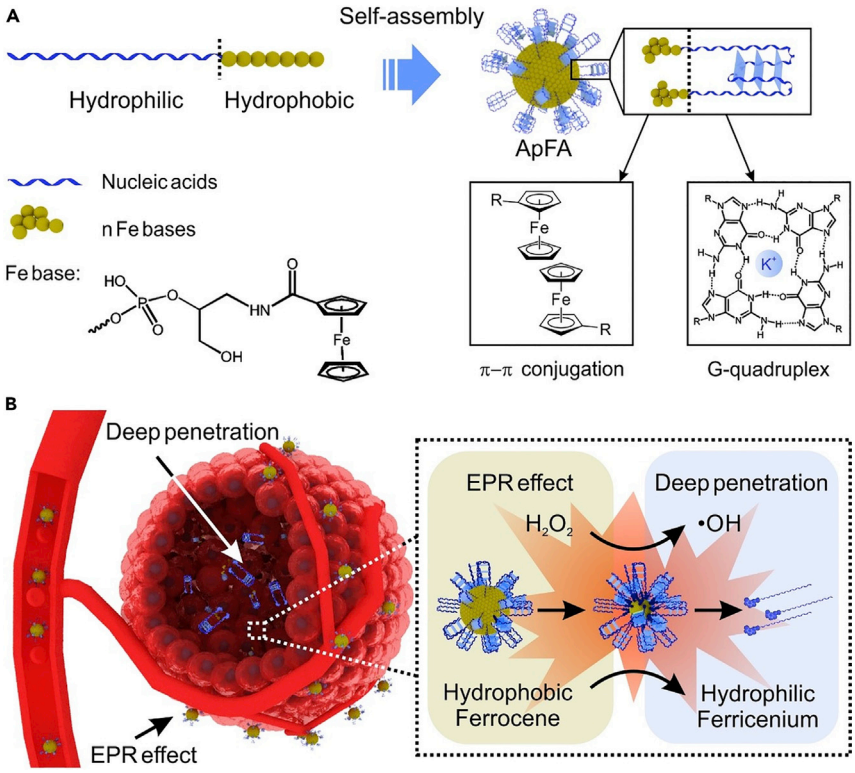


**Figure 1. Fabrication and Deep Penetration Schematics of ApFAs**

(A) Schematic of ApFAs fabrication.

(B) Schematic of deep penetration of ApFAs.

hydrophilic/hydrophobic ratio of the amphiphilic nucleic acid polymers. Through the reaction, ApFAs can realize remarkable size reduction and end with disintegration (Figure 1B). The shrunken assemblies can thus penetrate and internalize into cancer cells with the assistance of aptamers.

Solid-phase synthesis of aptamer-$Fe_n$ with defined chemical sequence has been carried out in the 3′ to 5′ direction using the phosphoramidite method.[43] Specifically, the first base on 3′ is covalently bound to a solid support material and remains attached to the material, and nucleosides carrying 5′-phosphate groups are used as starting material. Each nucleotide carrying 5′-phosphomonoester groups is covalently attached by the same stepwise addition approach. At the end, the oligonucleotide exists with the 3′ end attached to the CpG and the 5′ end protected with a 4,4′-Dimethoxytrityl group. Fe base can be precisely introduced in the nucleic acid sequence using this solid-phase synthesis. In this work, Fe base was attached to the 5′ end of thymine to impart hydrophobicity to the hydrophilic nucleic acid polymer. Measured by electrospray ionization mass spectrometry (Figures S1–S5; Table S1), aptamer-$Fe_n$ amphiphilic polymers with different numbers of Fe bases were efficiently prepared to form ApFAs in aqueous solution (Figure 2A). The morphology of ApFAs formed by aptamer-$Fe_n$ was studied using transmission electron microscopy (TEM) and atomic force microscopy (AFM). As shown in Figures 2B, 2E, and S6, ApFAs were well dispersed with uniform morphology and size. This evidence supports the self-assembly of amphiphilic nucleic acid polymers. In addition, the size of the ApFAs gradually increases as the number of Fe bases in aptamer-$Fe_n$ molecules increases (Figure S7). The size distribution of ApFAs was further provided using

Please cite this article in press as: Tan et al., Size-Tunable Assemblies Based on Ferrocene-Containing DNA Polymers for Spatially Uniform Penetration, Chem (2019), https://doi.org/10.1016/j.chempr.2019.05.024



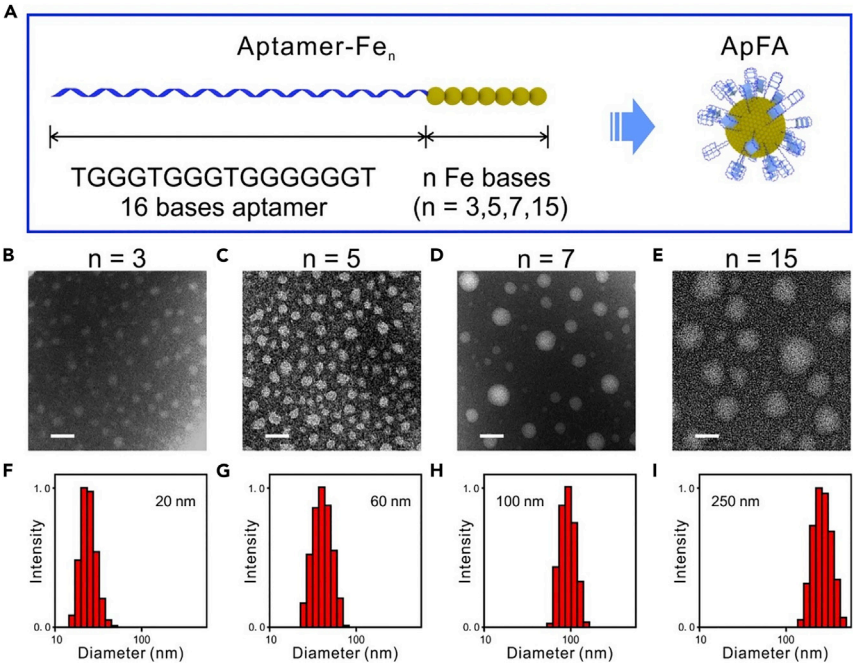


**Figure 2. Morphology and Size Distribution of ApFAs**

(A) Schematic of aptamer-Fe$_n$ amphiphilic molecules.

(B–E) TEM images of ApFAs formed by aptamer-Fe$_n$, n = 3 (B), 5 (C), 7 (D), and 15 (E), respectively. Scale bar, 100 nm.

(F–I) DLS data of ApFAs formed by aptamer-Fe$_n$, n = 3 (F), 5 (G), 7 (H), and 15 (I), respectively.

dynamic light scattering (DLS). It is clear that the hydrodynamic diameter of ApFAs increases from around 20 to 280 nm with the increase of n in the formula from 3 to 15 (Figures 2F–2I). As shown in Figure S8, the sizes of ApFAs had a negative correlation with the hydrophilic/hydrophobic ratio. The above results clearly show that the size of ApFA can be easily adjusted by changing the value of n in the aptamer-Fe$_n$ polymer.

## Size Shrinkage of ApFAs in Response to Tumor Microenvironment

A unique property of invasive cancers is altered glucose metabolism known as the Warburg effect.[44,45] The rapid growth and proliferation of tumors can lead to hypoxia, reactive oxygen species (ROS), and an acidic tumor microenvironment (pH 6.5–7.0).[46–48] Additionally, upon cellular uptake, pH gradients can even reach 5.0–6.0.[49] In the presence of oxidants under acidic conditions, hydrophobic ferrocene moieties in ferrocene derivatives can be easily oxidized into hydrophilic ferrocenium salts.[50–52] Consequently, ROS and acidic conditions in the tumor microenvironment have the intriguing potential to induce the size transformation of ApFAs. Under acidic conditions with $H_2O_2$, it is reasonable to speculate that the hydrophobic ferrocene moieties could be oxidized into hydrophilic $Fe(Cp)_2^+$, leading to size shrinkage of ApFAs (Figure 3A). ApFAs formed by aptamer-Fe$_7$ with the initial size of 100 nm were used here to fit the demands of the EPR effect.[53–55] The Fenton-like reaction-mediated size reduction of ApFAs was confirmed using TEM (Figures 3B–3D and S9) and AFM (Figure S10) under acidic and neutral conditions (pH 7.4–6.0). To investigate the response of ApFAs to the tumor microenvironment, $H_2O_2$ and acidic conditions were employed in a solution of ApFAs in sequence. For ApFAs formed at pH 7.4 (Figure 3B), assemblies with a uniform

Please cite this article in press as: Tan et al., Size-Tunable Assemblies Based on Ferrocene-Containing DNA Polymers for Spatially Uniform Penetration, Chem (2019), https://doi.org/10.1016/j.chempr.2019.05.024



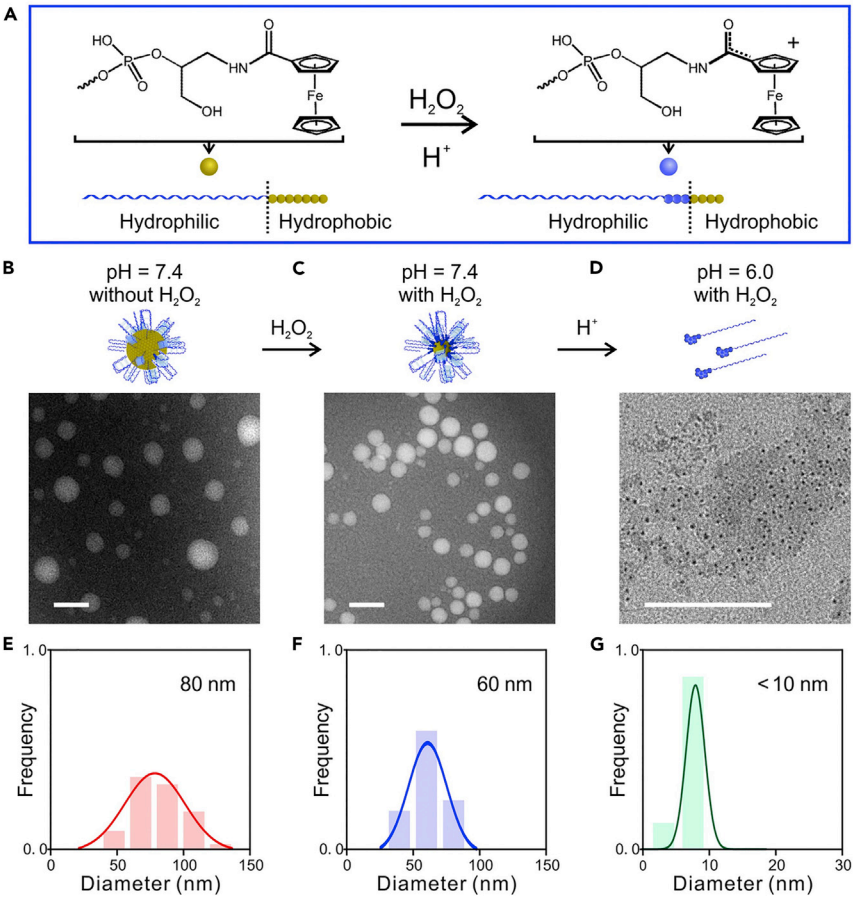


**Figure 3. Construction and Physicochemical Properties of ApFAs Formed by Aptamer-$Fe_7$ before and after Oxidation**

(A) Schematic of assembled size reduction via Fenton-like reaction.

(B–G) TEM images (B–D) and corresponding size distributions (E–G) of ApFAs at different conditions. Shown in (B) and (E) are ApFAs treated without $H_2O_2$ at pH 7.4. Shown in (C) and (F) are ApFAs treated with $H_2O_2$ at pH 7.4 for 5 min. (D and G) ApFAs treated with $H_2O_2$ at pH 6.0 for 5 min. Scale bar, 100 nm.

morphology were formed. When $H_2O_2$ was added to the solution, assemblies with spherical morphology could also be clearly observed, suggesting that $H_2O_2$ has low oxidation activity to aptamer-$Fe_7$ under neutral conditions (Figure 3C). Then, when the pH value was changed to 6.0, small-sized particles were observed (Figure 3D). Moreover, the corresponding size distributions of ApFAs were determined (Figure S11), and the size of ApFAs reduced from about 100 to 10 nm (Figures 3E–3G). To particularly explore the response of ApFAs at different conditions *in vivo*, the contraction of ApFAs was characterized over a range of pH gradients without and with $H_2O_2$ (Figure S12). The TEM images and corresponding size distributions of ApFAs indicated that ApFAs will experience an obvious shrinkage at pH 6.5 and 6.0. The stability of ApFAs with $H_2O_2$ at pH 7.4 was also evaluated using TEM (Figure S13), and the result showed that it took 4–8 h for ApFAs to shrink from 100 to 20 nm at pH 7.4 with $H_2O_2$. This result further illustrates that ApFAs can selectively shrink in an acidic tumor microenvironment. All these results indicate that the size of ApFAs can be triggered by the tumor microenvironment to undergo sharp shrinkage, which supports the speculation that the size shrinkage of ApFAs depends on their response to the tumor microenvironment.

Please cite this article in press as: Tan et al., Size-Tunable Assemblies Based on Ferrocene-Containing DNA Polymers for Spatially Uniform Penetration, Chem (2019), https://doi.org/10.1016/j.chempr.2019.05.024



### *In Vitro* Anticancer Activity of G-ApFAs

Fe (II) and Fe (III) can undergo a Fenton reaction under acidic conditions.[38,56,57]

$$Fe^{2+} + H_2O_2 \rightarrow Fe^{3+} + OH^- + \bullet OH \quad \text{(Equation 1)}$$

$$Fe^{3+} + H_2O_2 \rightarrow Fe^{2+} + H^+ + \bullet OOH \quad \text{(Equation 2)}$$

During the Fenton reaction, 3,3′,5,5′-tetramethyl-benzidine (TMB) was used to monitor hydroxyl radical production. The produced hydroxyl radicals from $H_2O_2$ can oxidize colorless TMB to chromogenic TMB cation-free radicals. Based on the aforementioned principles, typical Michaelis-Menten steady-state kinetics were observed (Figures 4A–4C). The time-course absorbance upon the addition of $H_2O_2$ into ApFAs was plotted in Figure 4A, and the corresponding Michaelis-Menten curve was calculated (Figure 4B). Photographs in the inset of Figure 4B visually present the chromogenic changes after the addition of $H_2O_2$. Specifically, the absorbance declined as the concentration of $H_2O_2$ increased in the acidic environment, and the results showed that ApFAs can dramatically escalate the concentration of hydroxyl radicals owing to the Fenton-like reaction. Furthermore, to determine the Michaelis-Menten constant ($K_M$) and maximum velocity ($V_{max}$), a linear double-reciprocal plot was prepared (Figure 4C), and the $K_M$ and $V_{max}$ values for ApFAs were calculated to be 1.4 mM and $7.9 \times 10^{-7}$ M $s^{-1}$, respectively. During the Fenton-like reaction, the Fe (II) in ferrocene moieties could partially be oxidized into hydrophilic Fe (III) that is known to shorten the transverse relaxation time of water protons, and Fe (III) can be used as a negative contrast agent in MRI.[32–34] As shown in Figure 4D, the signal intensity of T2-weighted phantom images clearly decreased in $H_2O_2$-treated ApFAs sample, but the MR signal did not change in non-$H_2O_2$ samples or aptamer samples, indicating that the $H_2O_2$-oxidized ApFAs can be used as a contrast enhancer in T2-weighted MRI. The MR images of the $H_2O_2$-oxidized ApFAs also exhibited a concentration-dependent darkening phenomenon. These results illustrate the negative contrast enhancement of MR signal by the oxidized ApFAs (Figures 4E and 4F). This cumulative evidence supported that ApFAs can perform Fenton-like reaction with significant hydroxyl radical formation and Fe (III) production in an acidic environment. Tumor-site-specific generation of hydroxyl radicals was reported to induce the apoptosis of cancer cells.[35–39] As a result, ApFAs can be considered as potential antitumor therapeutic agents, while normal cells incubated with ApFAs would be left unharmed.[58]

The tumor microenvironment contains significant glucose for tumor proliferation,[59,60] and the glucose can be catalyzed into $H_2O_2$ by GOD.[61] Sequentially, ApFAs can catalyze the disproportionation of $H_2O_2$ and generate highly toxic hydroxyl radicals in the acidic tumor environment. In contrast, ApFAs and $H_2O_2$ can produce nontoxic $H_2O$ and $O_2$ in a neutral environment. The cytotoxicity profiles of G-ApFAs were evaluated by CCK8 (Figure 4G) and Annexin V-PI (Figure S14) under both acidic (pH = 6.0) and neutral (pH = 7.4) conditions. Cell viability was found to be highly dependent on the dosage of G-ApFAs and the pH value. As shown in Figure 4G, G-ApFAs presented about 70% of cell viability at 0.5 μM under acidic condition, while much higher cell viability (95%) could be observed at corresponding concentrations under neutral conditions. The cytotoxicity of ApFAs was also verified by Annexin V-PI (Figure S14), and the results matched well with that evaluated by CCK8. To demonstrate the production of ROS, a ROS fluorescence probe 2′,7′-dichlorofluorescin diacetate (DCFH-DA) was used to stain A549 cells treated with phosphate-buffered saline (PBS), ApFAs, and G-ApFAs under neutral

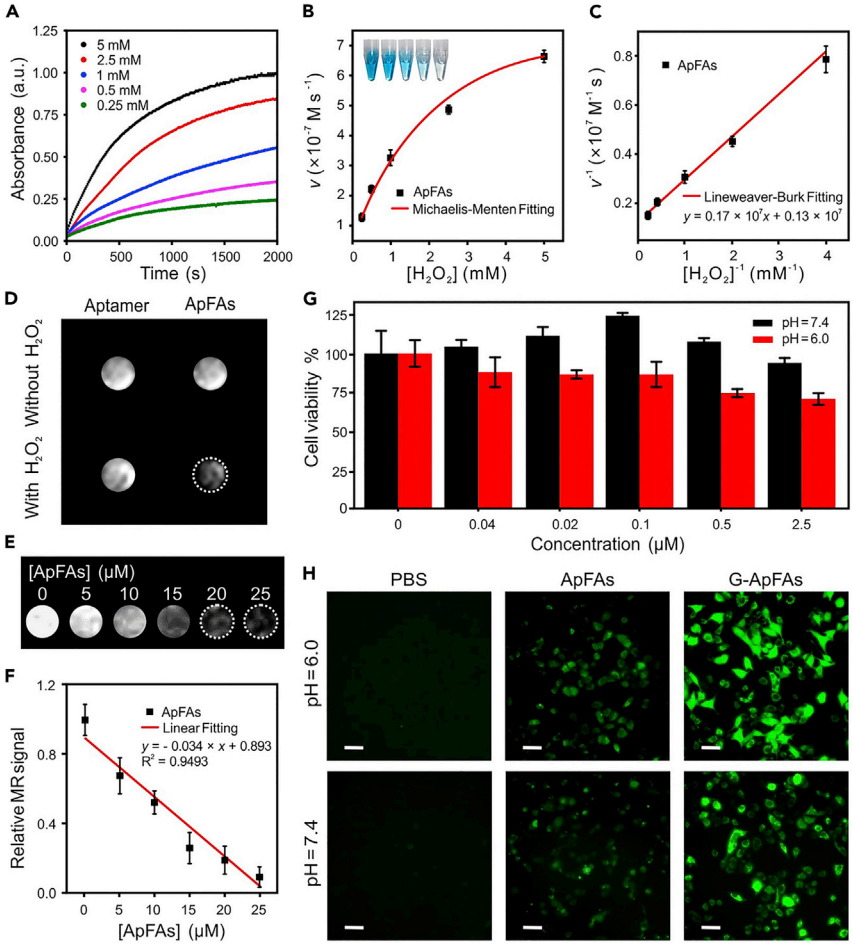


**Figure 4. *In Vitro* Characterizations of the Catalytic Performance and Anticancer Activity of ApFAs**

(A) Time-course absorbance of ApFAs upon the addition of $H_2O_2$ at varied concentrations.

(B and C) Shown in (B) are Michaelis-Menten kinetics and in (C) a Lineweaver-Burk plot of ApFAs. Mean values and error bars are defined as mean and SD, respectively. Error bar indicates the SD; n = 8.

(D) T2-weighted MR images of aptamer S13 and ApFAs treated without and with $H_2O_2$ at pH 6.0.

(E) T2-weighted phantom images of $H_2O_2$-treated ApFAs at different concentrations.

(F) Corresponding quantitative data analysis of (E). Error bar indicates the SD; n = 3.

(G) Cytotoxicity of G-ApFAs (0.1 nM GOD in ApFAs) to A549 cells under both acidic (pH = 6.0; red) and neutral (pH = 7.4; black) conditions. Error bar indicates the SD; n = 5.

(H) Fluorescence microscope images of A549 cells after co-incubation with PBS, ApFAs, and G-ApFAs under neutral (pH = 7.4) and acidic (pH = 6.0) conditions for 4 h and subsequently stained with ROS fluorescence probe DCFH-DA. Scale bar, 50 μm.

and acidic conditions (Figure 4H). The green fluorescence was hardly observable in both PBS-treated cells and ApFAs-treated cells. Contrarily, a strong green signal could be observed in the G-ApFAs-treated cells at pH = 6.0, indicating the effective ROS production of G-ApFAs in the acidic environment. Comparatively, the fluorescence intensity of G-ApFAs-treated cells at pH 6.0 is approximately 1.5 times that of pH 7.4, and the results revealed less efficient ROS production under neutral conditions compared to acidic conditions (Figure S15). The above results demonstrate that Fenton-like reaction-performing G-ApFAs can amplify abundant hydroxyl radicals, leading to the death of cancer cells.

Please cite this article in press as: Tan et al., Size-Tunable Assemblies Based on Ferrocene-Containing DNA Polymers for Spatially Uniform Penetration, Chem (2019), https://doi.org/10.1016/j.chempr.2019.05.024



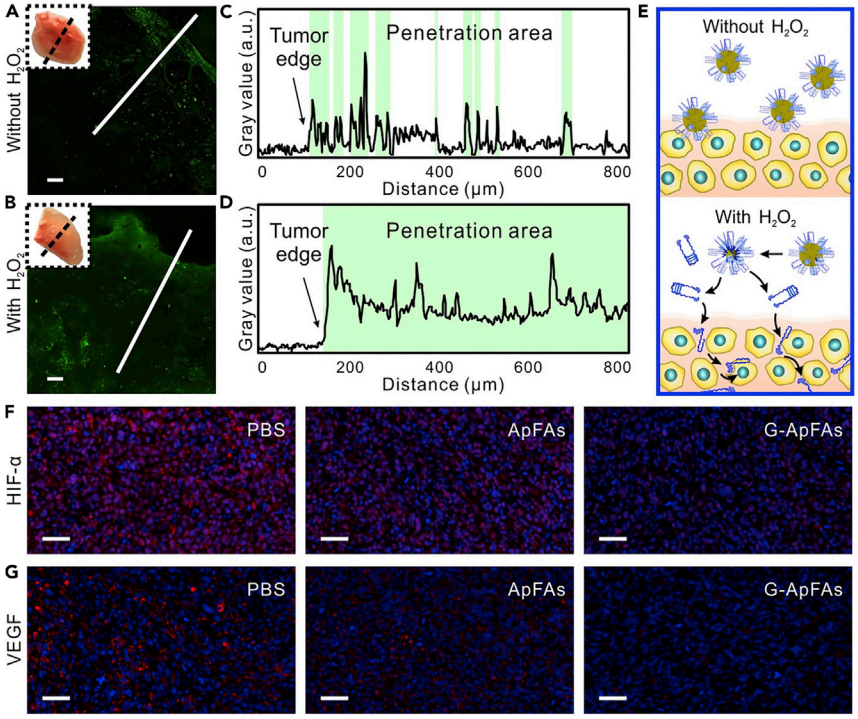


**Figure 5. Penetration of ApFAs toward Tumor Tissues**

(A and B) Penetration of FAM-ApFAs in tumor tissue after 2 h incubation (A) in PBS only and (B) in PBS with $H_2O_2$. Inset map is the physical map of tumor tissue (size: 4 mm × 4 mm × 4 mm), and the dotted black line shows the cross section of the tumor tissue. Scale bar, 100 μm.

(C and D) Variation of the gray value over the tissues indicated by the solid white line is shown in (C) and (D), respectively. The green area means ApFA-penetrated area (signal to noise ratio > 3).

(E) A proposed model for the tumor tissue penetration of ApFAs without and with $H_2O_2$.

(F and G) HIF-α (F) and VEGF (G) staining of A549 tumor xenografts after mice intravenously injected with PBS, ApFAs, and G-ApFAs, respectively. Scale bar, 50 μm.

## Tissue Penetration Ability of ApFAs

Based on the sharp size shrinkage of ApFAs from about 100 to 10 nm, the solid tumor penetration ability of ApFAs was further investigated using a solid tumor tissue derived from mice bearing A549 tumor xenografts under the conditions without and with $H_2O_2$. For tumor tissue incubated with 5-carboxyfluorescein-labeled ApFAs (denoted as FAM-ApFAs), green fluorescence from 5-Carboxyfluorescein dye (FAM) was mostly dispersed at the periphery of tumor tissue, and little signal could be detected in the center (Figure 5A), indicating that ApFAs could not penetrate into the central portion of solid tumor tissues without the assistance of oxidant. In contrast, the emitted green signals were much deeper and stronger inside the tumor tissue after co-incubation with FAM-ApFAs and $H_2O_2$ (Figure 5B), suggesting an improved tumor penetration of ApFAs. Quantitative evaluation on the penetration ability of ApFAs is shown in Figures 5C and 5D; the higher gray value means the stronger fluorescence intensity, suggesting more fluorescent labeled molecules penetrate to the position. The penetration area is labeled in green, and it also indicates spatially uniform tumor penetration of ApFAs under $H_2O_2$ condition. The biocompatibility and aptamer-mediated internalization of ApFAs were further confirmed by cytotoxicity assay (Figure S16), confocal laser scanning microscopy (Figures S17 and S18), and flow cytometry analysis (Figure S19). The proposed model for the penetration behavior of ApFAs is shown in Figure 5E. Without the aid of oxidant, ApFAs with a

Please cite this article in press as: Tan et al., Size-Tunable Assemblies Based on Ferrocene-Containing DNA Polymers for Spatially Uniform Penetration, Chem (2019), https://doi.org/10.1016/j.chempr.2019.05.024



large initial size were hindered by the dense collagen matrix in tumor tissues. In contrast, with the presence of oxidant, ApFAs could realize remarkable size shrinkage by Fenton-like reaction, and the shrunken assemblies could penetrate and internalize into cancer cells with the help of aptamers (Figure 5E). As shown in Figure S20, the T2-weighted MR images of G-ApFAs-treated mice exhibited a darkening phenomenon in tumor sites, and this phenomenon demonstrates the massive generation of Fe (III) by G-ApFAs *in vivo*. The variation of MR signal value further clarifies that G-ApFAs show spatially uniform tumor penetration ability *in vivo* (Figure S21). These results indicate that the penetration and internalization performance of ApFAs can be attributed to the tumor-microenvironment-responsive shrinkage of ApFAs, suggesting the potential capability of ApFAs to deliver anticancer agents into deep tumor tissues.

Rapid proliferation of tumor cells leading to the hypoxia in tumor tissues.[44,45] The highly toxic hydroxyl group can efficiently kill tumor cells, slow down the proliferation of tumor cells, and thereby inhibit the hypoxia of tumor tissues.[62,63] As a kind of highly active oxygen-containing radical, a hydroxyl radical can also participate in the hydroxylation reaction, leading to the degradation of HIFα.[64,65] Additionally, hydroxyl radicals and superoxide radicals were reported to undergo electron-transfer reactions and generate oxygen, thereby inhibiting hypoxia in the tumor area.[66] To further study the inhibition of hypoxia, a corresponding immunofluorescence assay was performed. As two hypoxia-associated markers, hypoxia-inducible factor-α (HIF-α) and vascular epithelial growth factor (VEGF) were chosen to verify hypoxia status of tumor tissues. HIF-α is reported as a downstream marker of hypoxia, and VEGF is well known as a downstream target of HIF-α.[60] The downregulation of HIF-α and VEGF has been generally regarded as a phenomenon of the inhibition of tumor hypoxia.[67] As shown in Figure 5F, HIFα-staining images could hardly display any red fluorescence of HIF-α in the G-ApFAs-treated group compared with the PBS-treated group and ApFAs-treated group. At the same time, the PBS-treated group exhibited extremely vivid red signal of VEGF as well as ApFAs-treated group (Figure 5G), demonstrating the high expression of VEGF owing to the tumor hypoxia. Comparatively, weak VEGF signal could be observed in the G-ApFAs-treated group. The down-regulation of HIF-α and VEGF in G-ApFAs-treated group reveals the G-ApFAs-mediated inhibition of tumor hypoxia. As proved both *in vitro* and *in vivo*, G-ApFAs show excellent ability to generate hydroxyl radicals and Fe (III) in the tumor microenvironment.

### *In Vivo* Therapeutic Efficacy of G-ApFAs

The *in vivo* antitumor efficacy of G-ApFAs was further systematically studied. First, the extended blood circulation and enhanced tumor accumulation of G-ApFAs were evaluated in A549 tumor-bearing mice and monitored by fluorescence imaging. After the tumor had developed, Cy5-labeled G-ApFAs and free GOD mixed with Cy5-labeled random DNA-Fe oligos unable to form an assembly structure (denoted as Cy5-labeled G-rDNA-Fe) were intravenously injected into mice bearing a subcutaneous A549-cell-derived xenograft tumor. Cy5-labeled G-ApFAs had almost the same size and stability as unlabeled ApFAs (Figure S22), indicating that conjugation with Cy5 did not affect assembly formation. When Cy5-labeled G-ApFAs were injected into A549-tumor-bearing BALB/c nude mice through the tail vein, an obvious fluorescence signal could be observed at the tumor site (Figure 6A). In contrast, after 4 h post injection of Cy5-labeled G-rDNA-Fe, little fluorescence signal could be observed at the tumor site within the extended observation time window (Figure 6B). Therefore, it can be concluded that G-ApFAs possess better tumor accumulation capability compared to G-rDNA-Fe. The fluorescence signal

Please cite this article in press as: Tan et al., Size-Tunable Assemblies Based on Ferrocene-Containing DNA Polymers for Spatially Uniform Penetration, Chem (2019), https://doi.org/10.1016/j.chempr.2019.05.024



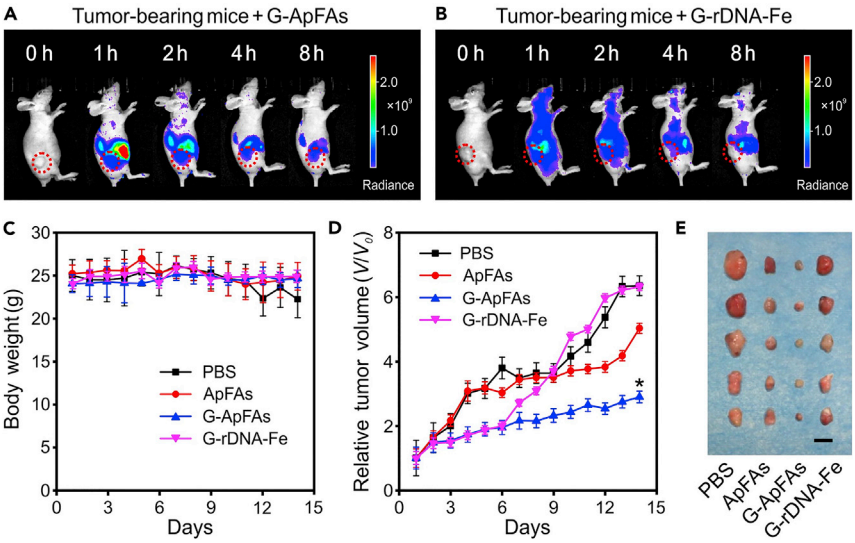


**Figure 6. *In Vivo* Therapeutic Efficacy of G-ApFAs**

(A and B) Time-dependent fluorescence images of A549 tumor-bearing mice after intravenous injection of (A) Cy5-labeled G-ApFAs and (B) Cy5-labeled G-rDNA-Fe.

(C) The body weights of nude mice bearing A549 tumor xenografts after injection with PBS, ApFAs, G-ApFAs, and G-rDNA-Fe via the intratumoral route (all injections were equivalent to 5.0 mg $kg^{-1}$). Error bar indicates the SD; n = 5.

(D) The tumor volumes of A549-bearing nude mice treated with PBS, ApFAs, G-ApFAs, and G-rDNA-Fe administered via the intratumoral route. All the above data were collected and measured every day. Statistical significance was assessed by Student's two-sided t test compared to the PBS group. Asterisks (*) denote the statistical significance for *$p < 0.05$. Error bar indicates the SD; n = 5.

(E) Digital photographs of the dissected tumors after 14 days of therapy. Scale bar, 10 mm.

of Cy5-labeled G-ApFAs lasted for more than 24 h (Figures S23 and S24), and the real-time tumor accumulation showed that the total fluorescence signal in G-ApFAs-treated mice tumor is notably higher than that in mice treated with G-rDNA-Fe (Figure S25). The pharmacokinetic parameter of G-ApFAs was also characterized, and half-life $t_{1/2}$ was about 6 h (Figure S26). These combined results demonstrate that G-ApFAs are stable enough to circulate in the bloodstream and passively target tumors. Additionally, fluorescence signals of *ex vivo* tumor tissues and major organs can also be observed at the $24^{th}$ h (Figure S27), and the results can also verify the tumor accumulation of G-ApFAs after intravenous injection. It has been reported that large particles (>100 nm) could be rapidly trapped in the liver, while small particles (<10 nm) tend to be eliminated through the kidney.[68,69] As shown in Figure S27, fluorescence signals from G-ApFAs can be clearly observed in the liver and kidneys, indicating that G-ApFAs could be metabolized through the liver and kidneys. However, the fluorescent signal from G-rDNA-Fe appeared only in the kidneys, indicating that G-rDNA-Fe was only metabolized through the kidneys. This result further demonstrates the size-tunability of G-ApFAs from larger than 100 nm to less than 10 nm during drug delivery *in vivo*.

Next, the therapeutic performance of G-ApFAs was investigated in A549-tumor-bearing mice. After the tumors had developed to approximately 30 $mm^3$, mice were randomly divided into four groups (n = 5) in order to minimize weight and differences in tumor size. PBS, ApFAs, G-ApFAs, and G-rDNA-Fe were administered via the intratumoral route to investigate therapeutic performance, respectively. During the 14 days of the therapeutic period, the body weights of mice in control and all therapeutic groups showed no significant variations (Figure 6C), indicating

Please cite this article in press as: Tan et al., Size-Tunable Assemblies Based on Ferrocene-Containing DNA Polymers for Spatially Uniform Penetration, Chem (2019), https://doi.org/10.1016/j.chempr.2019.05.024



that no significant toxicity had been induced by the injection of ApFAs or G-ApFAs during treatment. Upon tumor suppression assessments, G-ApFA administrations presented satisfactory suppressive effect (Figure 6D). More specifically, according to the variation of the relative tumor weight, the suppression rates of G-ApFAs were calculated as 90%. Notably, the tumor volume of mice treated with G-rDNA-Fe increased slowly at first, and then a sharp rise was observed, as shown in Figure 6D. Initially, the depletion of tumor-reliant glucose and the poor oxygen supply could drive hypoxic regions into anoxia and death.[70,71] Then, the accumulation of $H_2O_2$ molecules produced by the free GOD in G-rDNA-Fe was reported to promote tumor heterogeneity, invasion, and metastasis, leading to the acceleration of tumor growth.[72] After administration of the therapeutic protocol, tumors of mice in all groups were dissected. As shown in Figure 6E, tumors from G-ApFAs-treated mice had a small volume, visually demonstrating that A549 tumor growth can be effectively suppressed after the administration of G-ApFAs. The satisfactory effect of tumor suppression by G-ApFAs can be attributed to the spatially uniform distribution of G-ApFAs in the tumor site and the production of highly toxic hydroxyl radicals. G-ApFAs can be effectively delivered to the tumor tissue to produce massive $H_2O_2$ through subsequent chemo-catalytic Fenton-like reactions. The toxic hydroxyl radicals could then kill cancer cells through a mitochondria-mediated apoptosis pathway.[73] The above results demonstrate the substantial *in vivo* efficacy of G-ApFAs in tumor therapy. Histological examination of tumors was performed to further confirm the therapeutic efficacy of G-ApFAs. Anticancer effects of G-ApFAs were evidenced by the irregular widening of intercellular space observed in tumor tissues (Figure 6F). As presented in Figure S28, each kind of organ isolated from mice in the four groups shows similar weights, and these results could clarify the good biocompatibility of ApFAs and G-ApFAs. The histological changes of major organs were also examined by H&E staining. The kidney, liver, and spleen of mice displayed no obvious abnormalities or lesions in all groups (Figure S29), indicating that ApFAs and G-ApFAs exert limited adverse side effects to organs.

## DISCUSSION

In this work, by using amphiphilic ferrocene-containing nucleic acid polymers, a size-tunable ApFA system was developed to resolve the size conflict between the EPR effect and spatially uniform tumor penetration. Initial ApFAs can accumulate at the tumor site via the EPR effect. When exposed to the tumor microenvironment, ApFAs can then undergo Fenton's reaction to achieve a remarkable size reduction from 100 to 10 nm, leading to improved tumor penetration ability of the assemblies. ApFAs can also release highly toxic hydroxyl radicals in the tumor microenvironment, achieving cancer treatment based on the catalytic reaction. Overall, ApFAs not only represent a drug delivery system featuring EPR effect and tumor penetration ability but also provide a promising step toward biopharmaceutics for cancer treatment.

## EXPERIMENTAL PROCEDURES

### Materials and Reagents

All reagents were used as received from commercial sources or prepared as described in references. All DNA synthesis reagents were purchased from Glen Research (Sterling, VA). Protected Fe base was synthesized in our lab.

Dulbecco's phosphate-buffered saline (DPBS), Dulbecco's modified Eagles medium (DMEM), Leibovitz's L-15 medium (L-15) and fetal bovine serum (FBS) were obtained from Thermo Fisher Scientific, Inc. All solutions used in the experiments were

Please cite this article in press as: Tan et al., Size-Tunable Assemblies Based on Ferrocene-Containing DNA Polymers for Spatially Uniform Penetration, Chem (2019), https://doi.org/10.1016/j.chempr.2019.05.024



prepared using ultrapure water (resistance > 18 MΩ cm), which was obtained through a Millipore Milli-Q ultrapure water system (Billerica, MA, USA).

### Synthesis of Fe Base

The synthesis of the Fe base is as described. Briefly, commercially available (S)-3-amino-1, 2-propanediol was coupled with ferrocene carboxylic acid, and the corresponding phosphoramidite compound (Figure S1) was prepared for DNA solid-phase synthesis.

### Fe-Base Characterization

Anhydrous solvent pyridine, $CH_3CN$, $CH_2Cl_2$, and N,N-Dimethylformamide were distilled under a nitrogen atmosphere and stored with 4 Å molecular sieves. $^1H$ spectra were recorded on a Bruker AM300 spectrometer. $^{13}C$ NMR spectra were recorded on a Bruker AM400 spectrometer. Chemical shifts (δ) are reported in ppm, and coupling constants (J) are in Hertz (Hz). The following abbreviations were used to explain the multiplicities: s = singlet, d = doublet, t = triplet, q = quartet, m = multiplet, br = broad.

$^1H$ NMR: 7.49 (d,2H, J-7.6Hz ), 7.37–7.35 (d,4H, J-8.4Hz), 7.31–7.18 (m,3H), 6.84–6.79 (m,4H), 6.23 (t,0.59H, J-5.2Hz), 6.03 (t, 0.31H, J-5.2Hz), 4.61 (s,0.63H), 4.53 (s, 1.23H), 4.28 (s, 2H), 4.11–4.11 (s, 5.57H), 3.89–3.81 (m,1.38H), 3.74–3.48 (m, 10.74H), 3.32–3.26 (m,2H), 2.6 (t,1.25H, J-6.2Hz), 2.45 (t,0. 67H, J-6.2Hz), 2.1 (s,1H), 1.29–1.12 (m,12H).

$^{13}C$ NMR: 170.09, 158.51, 144.74, 135.86, 130.10, 128.01. 127.48, 126.40, 117.69, 113.17, 86.24, 72.51, 72.36, 70.29, 70.13, 69.66, 68.50, 68.27, 67.87, 67.55, 64.88, 64.57, 60.35, 58.45, 58.28, 58.10,55.18, 24.68, 21.02,20.40, 20.25, 14.19.

$^{31}P$ NMR δ: 149.68, 148.72.

MS (ESI+): m/z 828.30 [M + Na].

### DNA Synthesis

All DNA oligonucleotides (Table S1) were synthesized using standard phosphoramidite chemistry on controlled pore glass supports on an ABI 394 DNA Synthesizer. The oligonucleotides were designed to have 16 natural bases and several Fe bases. Coupling times were 60 s. The completed sequences were then deprotected in saturated ammonium hydroxide at room temperature for 12 h and further purified by reversed-phase high-performance liquid chromatography (HPLC) (ProStar; Varian) on a C18 column using 0.1 M triethylammonium acetate (TEAA) buffer (Glen Research) and acetonitrile (Sigma Aldrich) as the eluents. The collected DNA products were dried and detritylated by dissolving and incubating DNA products in 200 μL of 80% acetic acid for 20 min. The detritylated DNA product was precipitated with NaCl (3 M; 25 μL) and ethanol (600 μL) and then desalted using Sep-Pac Plus C18 cartridges. The obtained oligonucleotides were quantified by measuring their absorbance at 260 nm and characterized by electrospray ionization mass spectrometry (Figures S2–S5).

### Preparation of ApFAs and G-ApFAs

ApFAs with G-quadruplex were formed by hydrophobic self-assembly of aptamer-$Fe_n$ oligonucleotides in DPBS solution (5 mM $Mg^{2+}$). Briefly, the desalted aptamer-$Fe_n$ oligonucleotides were diluted with DPBS buffer (5 mM $Mg^{2+}$) to the desired concentration, left at room temperature for about an hour, and then used

Please cite this article in press as: Tan et al., Size-Tunable Assemblies Based on Ferrocene-Containing DNA Polymers for Spatially Uniform Penetration, Chem (2019), https://doi.org/10.1016/j.chempr.2019.05.024



for subsequent experiments. G-ApFAs were formed by co-incubation with 0.1 nM GOD.

### ApFAs Characterization

ApFAs were diluted to 5 μM in DPBS (5 mM $Mg^{2+}$) buffer, and 10 μL of this solution was deposited on the freshly cleaved mica surface and allowed to adsorb for 5 min. Then, 10 μL of Millipore water was dropped on the surface and removed with filter paper. The mica surface was then washed twice with a further 20 μL of Millipore water and dried by nitrogen gas prior to imaging. TEM images were obtained after negative staining with 1% aqueous uranyl acetate by using a transmission electron microscope (Hitachi H-7000). The TEM samples were dropped onto standard holey carbon-coated copper grids. The particle sizes (diameters) and their distribution were measured by a ZetaPALS DLS detector at 25°C. The scattering angle was fixed at 90°.

### Cell Culture

A549 cells were cultured in RPMI DMEM medium supplemented with 10% FBS (Zeta). Cells were maintained at 37°C in a humidified atmosphere containing 5% $CO_2$ with medium renewal every 2 days.

### Cytotoxicity Assay

The cytotoxicity of ApFAs was determined using a CellTiter 96 cell proliferation assay (Promega, Madison, WI, USA). After seeding in 96-well plates and culturing overnight, the cells were incubated with ApFAs (with a final concentration ranging from 0.004 to 2.5 μM, diluted by culture media) for 2 h, washed with PBS, and then cultured with fresh medium for future cell growth (48 h). After removing the cell medium, CellTiter reagent (20 μL) diluted in fresh medium (100 μL) was added to each well and incubated for 1–2 h. The absorbance (490 nm) was recorded by using a plate reader (Tecan Safire microplate reader, AG, Switzerland). Cell viability was determined as described by the manufacturer.

### ROS Detection

For ROS observations on microscopy, A549 cancer cells were plated on a 35 mm culture dish for 24 h, and a 2′,7′-DCFH-DA probe was used to detect intracellular ROS. Subsequently, the culture dish was rinsed with PBS twice before 1 mL of DMEM high-glucose (at pH 7.4 or 6.0) containing 10 μmol $L^{-1}$ of G-ApFAs and ApFAs was replaced and co-incubated for 4 h. The medium was then removed by PBS followed by the addition of DCFH-DA probe. Herein, 10 μmol $L^{-1}$ non-fluorescent DCFH-DA was applied for 30 min, forming fluorescent matter 2′,7′-Dichlorofluorescein (DCF) ($\lambda_{ex}$ = 480 nm; $\lambda_{em}$ = 525 nm) that can be observed by fluorescence microscopy.

### Confocal Fluorescence Imaging

A549 cells were plated on a 35 mm confocal laser culture dish for 24 h. FAM-labeled ApFAs or random DNA-Fe (final concentration of 300 nM) was respectively delivered into A549 cells at 37°C for 1 h. After washing with DPBS three times, confocal fluorescence imaging studies were performed on the FV1000 confocal laser scanning microscope. Imaging of the cells was performed on an Olympus FV500-IX81 confocal microscope (Olympus America, Inc., Melville, NY). A 5 mW 488 nm Argon ion laser was the excitation source throughout the experiments. The objective used for imaging was a PLAPO60XO3PH 60× oil immersion objective with a numerical aperture of 1.40 from Olympus (Melville, NY).

Please cite this article in press as: Tan et al., Size-Tunable Assemblies Based on Ferrocene-Containing DNA Polymers for Spatially Uniform Penetration, Chem (2019), https://doi.org/10.1016/j.chempr.2019.05.024



### Gel Electrophoresis Assay

Polyacrylamide gel electrophoresis was used to analyze the stability of ApFAs after samples were incubated with 10% FBS. Twenty μL samples were mixed with 4 μL 6× loading buffer and then loaded into 18% polyacrylamide gel in electrophoresis buffer (9 mM Tris; pH 8.0; containing 9 mM boric acid and 1 mM EDTA). After electrophoresis, the gels were analyzed with a molecular imager (BIO-RAD).

### Penetration of ApFAs toward Tumor Tissue

The tumor penetration ability of FAM-ApFAs was evaluated using a solid tumor tissue derived from mice bearing A549 tumor xenografts. The size of tumor tissue was about 4 × 4 × 4 mm and the tissues were divided into two equal parts before incubation. These two parts were then incubated with FAM-ApFAs (final concentration of 500 nM) in PBS solution with and without $H_2O_2$ at 37°C for 2 h. After washing with DPBS three times, confocal fluorescence imaging studies were performed on the FV1000 confocal laser scanning microscope. Imaging of the tissues was performed on an Olympus FV500-IX81 confocal microscope (Olympus America, Inc., Melville, NY). A 5 mW 488 nm Argon ion laser was the excitation source throughout the experiments. The cross-sectional analysis of fluorescence images was done using ImageJ software.

### *In Vivo* Fluorescence Imaging

All the experimental protocols involving animals were approved by Hunan University Laboratory Animal Center, and all mice received humane care in compliance with the Guide for the Care and Use of Laboratory Animals. Four-week-old female athymic BALB/c mice (Hunan Laboratory Animal Co., Ltd.) received a subcutaneous injection of 6 × 106 A549 cells into the right backside. Either 4.5 nmol Cy5-labeled G-ApFAs or G-rDNA-Fe (G-rDNA-Fe cannot assemble) was injected intravenously via the tail vein when tumor volume reached 20 to 30 $mm^3$ after mice were anesthetized with breathing oxygen and the anesthetic isopentane. Mouse tumor and other major organs were collected and measured for fluorescence intensity with an excitation bandpass filter at 535/30 nm and an emission at 610/75 nm.

### *In Vitro* Magnetic Resonance Imaging

All the *in vitro* T2-weighted magnetic resonance images were acquired using a 1.5 T small animal MRI scanner (at 37°C) with the following parameters: coil type, spiral coil; Tr, 2 s; Te, 56 ms; the average, 3; field of view, 35 × 45 mm; matrix size, 256 × 256; slice thickness, 1.2 mm; scan duration, 2 min; resolution, 0.16 × 0.16 mm; flip angle, 90°; software for acquisition and analysis and the duration of imaging, shinning MRI.

### *In Vivo* Magnetic Resonance Imaging

All the experimental protocols involving animals were approved by Hunan University Laboratory Animal Center, and all mice received humane care in compliance with the Guide for the Care and Use of Laboratory Animals. Four-week-old female athymic BALB/c mice (Hunan Laboratory Animal Co., Ltd.) received a subcutaneous injection of 6 × 106 A549 cells into the right backside. Either 4.5 nmol G-ApFAs or G-rDNA-Fe was injected intravenously via the tail vein when tumor volume reached 30 $mm^3$. After 0.5 h, mice were anesthetized through a single intraperitoneal injection of 10% chloral hydrate. MRI was performed at the desired time points after injection. A 1.5 T small animal MR scanner (60.875 MHz) was used to monitor the mice. All the *in vivo* T2-weighted magnetic resonance images were acquired using a 1.5 T small animal MRI scanner (at 37°C) with the following parameters: coil type, spiral coil; Tr, 500 ms; Te, 19.6 ms; the average, 3; field of view, 35 × 45 mm; matrix

size, 256 × 256; slice thickness, 1.2 mm; scan duration, 15 min; resolution, 0.16 × 0.16 mm; flip angle, 90°; software for acquisition and analysis and the duration of imaging, shinning MRI.

### *In Vivo* Therapeutic Efficacy

The tumors grew obviously on the fifth day post-injection of tumor cells. To assess the tumor growth inhibition effect by different treatments, female BALB/c mice bearing subcutaneous A549 tumors were randomly divided into four groups (n = 5) and subjected to variable conditions by intratumoral injection as follows: (1) PBS (control group), (2) ApFAs, (3) G-ApFAs (0.1 nM GOD loaded in ApFAs, therapeutic groups), and (4) G-rDNA-Fe (G-rDNA-Fe cannot assemble). Tumor size was measured by caliper every day according to the following formula:

$$\text{volume (V)} = (\text{tumor length}) \times (\text{tumor width})^2 / 2$$

The weight of mice was also measured every day. Then, these data were plotted as a function of time. To be more specific, the tumor inhibition rate was calculated based on the dissected tumor weight (wPBS – wG-ApFAs) / wPBS × 100%, rather than using tumor volume. Whereas wPBS refers to the average weight of tumors in the PBS group, wG-ApFAs refers to the average weight of tumors in the G-ApFAs-treated group.

### *In Vivo* Systemic Toxicity Assay

To evaluate the systemic toxicity, A549-tumor-bearing mice were sacrificed on the 14$^{th}$ day. Tumor and major organs, including heart, liver, lung, spleen, and kidney, were dissected after specific treatment and examined by H&E staining.

### Pharmacokinetic Parameter Characterization of G-ApFAs

Female mice (n = 3) were intravenously injected with G-ApFAs when they were 4 weeks old. At 2, 8, 15, and 30 min and 1, 2, 4, 8, and 24 h, 10 μL blood was drawn and dispersed into 990 μL physiological saline contained heparin sodium injection. The concentrations of Fe were measured by inductively coupled plasma optical emission spectrometer (ICP-OES). The *in vivo* circulating half-life of G-ApFAs in the bloodstream ($t_{1/2}$) is calculated.

### HIF-α and VEGF Staining

To further study the excellent overcoming hypoxia ability of G-ApFAs, the tumors were excised and collected on the 14$^{th}$ day. Then, the tumors of mice with different groups were fixed in 4% formalin for HIF-α and VEGF staining.

## SUPPLEMENTAL INFORMATION

Supplemental Information can be found online at https://doi.org/10.1016/j.chempr.2019.05.024.

A video abstract is available at https://doi.org/10.1016/j.chempr.2019.05.024#mmc2.

## ACKNOWLEDGMENTS

This work is supported by the Foundation for Innovative Research Groups of NSFC (21521063), the National Natural Science Foundation of China (21675120, 31701249, and 31601125), the NIH (GM R35 127130) and NSF (1645215), the National Key R&D Program of China (2017YFA0208000), the Natural Science Foundation of Hunan Province (2018JJ3037), and the Key Point Research and Invention Program of Hunan province (2017DK2011). This project is also funded by the China Postdoctoral Science Foundation.

## AUTHOR CONTRIBUTIONS

W.T., Q.Y., and J.T. conceived and designed the research; H.L., Z.S., and X.H. performed the *in vivo* experiments; R.A. and S.X. performed the synthesis; J.T., S.X., and L.Z. carried out the characterization experiments; M.Z. and Q.L. designed the diagrammatic drawing; Y.L. analyzed the data; Q.Y. and J.T. co-wrote the paper. All authors discussed the results and commented on the manuscript.

## DECLARATION OF INTERESTS

The authors declare no competing interests.

Received: February 12, 2019
Revised: April 16, 2019
Accepted: May 27, 2019
Published: June 13, 2019

## REFERENCES AND NOTES

1. Shi, J., Kantoff, P.W., Wooster, R., and Farokhzad, O.C. (2017). Cancer nanomedicine: progress, challenges and opportunities. Nat. Rev. Cancer *17*, 20–37.

2. Lammers, T., Kiessling, F., Hennink, W.E., and Storm, G. (2012). Drug targeting to tumors: principles, pitfalls and (pre-) clinical progress. J. Control. Release *161*, 175–187.

3. Torchilin, V.P. (2014). Multifunctional, stimuli-sensitive nanoparticulate systems for drug delivery. Nat. Rev. Drug Discov. *13*, 813–827.

4. Nishiyama, N., Matsumura, Y., and Kataoka, K. (2016). Development of polymeric micelles for targeting intractable cancers. Cancer Sci. *107*, 867–874.

5. Dong, R., Zhou, Y., Huang, X., Zhu, X., Lu, Y., and Shen, J. (2015). Functional supramolecular polymers for biomedical applications. Adv. Mater. *27*, 498–526.

6. Dai, Y., Xu, C., Sun, X., and Chen, X. (2017). Nanoparticle design strategies for enhanced anticancer therapy by exploiting the tumour microenvironment. Chem. Soc. Rev. *46*, 3830–3852.

7. Sun, T., Zhang, Y.S., Pang, B., Hyun, D.C., Yang, M., and Xia, Y. (2014). Engineered nanoparticles for drug delivery in cancer therapy. Angew. Chem. Int. Ed. *53*, 12320–12364.

8. Elsabahy, M., and Wooley, K.L. (2012). Design of polymeric nanoparticles for biomedical delivery applications. Chem. Soc. Rev. *41*, 2545–2561.

9. Cabral, H., Matsumoto, Y., Mizuno, K., Chen, Q., Murakami, M., Kimura, M., Terada, Y., Kano, M.R., Miyazono, K., Uesaka, M., et al. (2011). Accumulation of sub-100 nm polymeric micelles in poorly permeable tumours depends on size. Nat. Nanotechnol. *6*, 815–823.

10. Chen, J., Ding, J., Wang, Y., Cheng, J., Ji, S., Zhuang, X., and Chen, X. (2017). Sequentially responsive shell-stacked nanoparticles for deep penetration into solid tumors. Adv. Mater. *29*.

11. Jain, R.K., and Stylianopoulos, T. (2010). Delivering nanomedicine to solid tumors. Nat. Rev. Clin. Oncol. *7*, 653–664.

12. Wong, C., Stylianopoulos, T., Cui, J., Martin, J., Chauhan, V.P., Jiang, W., Popovic, Z., Jain, R.K., Bawendi, M.G., and Fukumura, D. (2011). Multistage nanoparticle delivery system for deep penetration into tumor tissue. Proc. Natl. Acad. Sci. U.S.A *108*, 2426–2431.

13. Perrault, S.D., Walkey, C., Jennings, T., Fischer, H.C., and Chan, W.C. (2009). Mediating tumor targeting efficiency of nanoparticles through design. Nano Lett. *9*, 1909–1915.

14. Sun, Q., Zhou, Z., Qiu, N., and Shen, Y. (2017). Rational design of cancer nanomedicine: nanoproperty integration and synchronization. Adv. Mater. *29*.

15. Savic, R., Luo, L., Eisenberg, A., and Maysinger, D. (2003). Micellar nanocontainers distribute to defined cytoplasmic organelles. Science *300*, 615–618.

16. Korevaar, P.A., George, S.J., Markvoort, A.J., Smulders, M.M., Hilbers, P.A., Schenning, A.P., De Greef, T.F., and Meijer, E.W. (2012). Pathway complexity in supramolecular polymerization. Nature *481*, 492–496.

17. Aliprandi, A., Mauro, M., and De Cola, L. (2016). Controlling and imaging biomimetic self-assembly. Nat. Chem. *8*, 10–15.

18. Nazemi, A., Boott, C.E., Lunn, D.J., Gwyther, J., Hayward, D.W., Richardson, R.M., Winnik, M.A., and Manners, I. (2016). Monodisperse cylindrical micelles and block Comicelles of controlled length in aqueous media. J. Am. Chem. Soc. *138*, 4484–4493.

19. Chen, H., Huang, Z.H., Wu, H., Xu, J.F., and Zhang, X. (2017). Supramolecular polymerization controlled through kinetic trapping. Angew. Chem. Int. Ed. *56*, 16575–16578.

20. Wilhelm, S., Tavares, A.J., Dai, Q., Ohta, S., Audet, J., Dvorak, H.F., and Chan, W.C.W. (2016). Analysis of nanoparticle delivery to tumours. Nat. Rev. Mater. *1*.

21. Chen, H.M., Zhang, W.Z., Zhu, G.Z., Xie, J., and Chen, X.Y. (2017). Rethinking cancer nanotheranostics. Nat. Rev. Mater. *2*.

22. Minchinton, A.I., and Tannock, I.F. (2006). Drug penetration in solid tumours. Nat. Rev. Cancer *6*, 583–592.

23. Su, L., Li, R.C., Khan, S., Clanton, R., Zhang, F.W., Lin, Y.N., Song, Y., Wang, H., Fan, J.W., Hernandez, S., et al. (2018). Chemical design of both a glutathione-sensitive dimeric drug guest and a glucose-derived nanocarrier host to achieve enhanced osteosarcoma lung metastatic anticancer selectivity. J. Am. Chem. Soc. *140*, 1438–1446.

24. Liu, K., Zheng, L., Ma, C., Göstl, R., and Herrmann, A. (2017). DNA-surfactant complexes: self-assembly properties and applications. Chem. Soc. Rev. *46*, 5147–5172.

25. Zhang, Y., Tu, J., Wang, D., Zhu, H., Maity, S.K., Qu, X., Bogaert, B., Pei, H., and Zhang, H. (2018). Programmable and multifunctional DNA-based materials for biomedical applications. Adv. Mater. *30*, e1703658.

26. Wu, Y., Sefah, K., Liu, H., Wang, R., and Tan, W. (2010). DNA aptamer-micelle as an efficient detection/delivery vehicle toward cancer cells. Proc. Natl. Acad. Sci. U. S. A *107*, 5–10.

27. Chen, T., Wu, C.S., Jimenez, E., Zhu, Z., Dajac, J.G., You, M., Han, D., Zhang, X., and Tan, W. (2013). DNA micelle flares for intracellular mRNA imaging and gene therapy. Angew. Chem. Int. Ed. *52*, 2012–2016.

28. Bang, S., Park, S., Lee, Y.M., Hong, S., Cho, K.B., and Nam, W. (2014). Demonstration of the heterolytic O-O bond cleavage of putative nonheme iron(II)-OOH(R) complexes for Fenton and enzymatic reactions. Angew. Chem. Int. Ed. *53*, 7843–7847.

29. Li, Y., Zhang, B., Liu, X., Zhao, Q., Zhang, H., Zhang, Y., Ning, P., and Tian, S. (2018).

Ferrocene-catalyzed heterogeneous Fenton-like degradation mechanisms and pathways of antibiotics under simulated sunlight: a case study of sulfamethoxazole. J. Hazard. Mater. *353*, 26–34.

30. Wang, Y., Yin, W., Ke, W., Chen, W., He, C., and Ge, Z. (2018). Multifunctional polymeric micelles with amplified Fenton reaction for tumor ablation. Biomacromolecules *19*, 1990–1998.

31. Mura, S., Nicolas, J., and Couvreur, P. (2013). Stimuli-responsive nanocarriers for drug delivery. Nat. Mater. *12*, 991–1003.

32. Hu, Y., Mignani, S., Majoral, J.P., Shen, M., and Shi, X. (2018). Construction of iron oxide nanoparticle-based hybrid platforms for tumor imaging and therapy. Chem. Soc. Rev. *47*, 1874–1900.

33. Crich, S.G., Terreno, E., and Aime, S. (2017). Nano-sized and other improved reporters for magnetic resonance imaging of angiogenesis. Adv. Drug Deliv. Rev. *119*, 61–72.

34. Li, Y., Hu, X., Ding, D., Zou, Y., Xu, Y., Wang, X., Zhang, Y., Chen, L., Chen, Z., and Tan, W. (2017). In situ targeted MRI detection of Helicobacter pylori with stable magnetic graphitic nanocapsules. Nat. Commun. *8*, 15653.

35. Huo, M., Wang, L., Chen, Y., and Shi, J. (2017). Tumor-selective catalytic nanomedicine by nanocatalyst delivery. Nat. Commun. *8*, 357.

36. Kwon, B., Han, E., Yang, W., Cho, W., Yoo, W., Hwang, J., Kwon, B.M., and Lee, D. (2016). Nano-Fenton reactors as a new class of oxidative stress amplifying anticancer therapeutic agents. ACS Appl. Mater. Interfaces *8*, 5887–5897.

37. Wlassoff, W.A., Albright, C.D., Sivashinski, M.S., Ivanova, A., Appelbaum, J.G., and Salganik, R.I. (2007). Hydrogen peroxide overproduced in breast cancer cells can serve as an anticancer prodrug generating apoptosis-stimulating hydroxyl radicals under the effect of tamoxifen-ferrocene conjugate. J. Pharm. Pharmacol. *59*, 1549–1553.

38. Huang, G., Chen, H.B., Dong, Y., Luo, X.Q., Yu, H.J., Moore, Z., Bey, E.A., Boothman, D.A., and Gao, J.M. (2013). Superparamagnetic iron oxide nanoparticles: amplifying ROS Stress to improve anticancer drug efficacy. Theranostics *3*, 116–126.

39. Lin, H., Chen, Y., and Shi, J. (2018). Nanoparticle-triggered in situ catalytic chemical reactions for tumour-specific therapy. Chem. Soc. Rev. *47*, 1938–1958.

40. Hu, J., Zhao, Z., Liu, Q., Ye, M., Hu, B., Wang, J., and Tan, W. (2015). Study of the function of G-rich aptamers selected for lung adenocarcinoma. Chem. Asian J. *10*, 1519–1525.

41. Liu, H.P., Moynihan, K.D., Zheng, Y.R., Szeto, G.L., Li, A.V., Huang, B., Van Egeren, D.S., Park, C., and Irvine, D.J. (2014). Structure-based programming of lymph-node targeting in molecular vaccines. Nature *507*, 519–522.

42. Jin, C., Liu, X.J., Bai, H.R., Wang, R.W., Tan, J., Peng, X.H., and Tan, W.H. (2017). Engineering stability-tunable DNA micelles using photocontrollable dissociation of an intermolecular G-quadruplex. ACS Nano *11*, 12087–12093.

43. Beaucage, S.L., and Iyer, R.P. (1992). Advances in the synthesis of oligonucleotides by the phosphoramidite approach. Tetrahedron *48*, 2223–2311.

44. Vander Heiden, M.G., Cantley, L.C., and Thompson, C.B. (2009). Understanding the Warburg effect: the metabolic requirements of cell proliferation. Science *324*, 1029–1033.

45. Hanahan, D., and Weinberg, R.A. (2011). Hallmarks of cancer: the next generation. Cell *144*, 646–674.

46. Xu, R., Zhang, G.D., Mai, J.H., Deng, X.Y., Segura-Ibarra, V., Wu, S.H., Shen, J.L., Liu, H.R., Hu, Z.H., Chen, L.X., et al. (2016). An injectable nanoparticle generator enhances delivery of cancer therapeutics. Nat. Biotechnol. *34*, 414–420.

47. Sabharwal, S.S., and Schumacker, P.T. (2014). Mitochondrial ROS in cancer: initiators, amplifiers or an Achilles' heel? Nat. Rev. Cancer *14*, 709–721.

48. Bristow, R.G., and Hill, R.P. (2008). Hypoxia and metabolism. Hypoxia, DNA repair and genetic instability. Nat. Rev. Cancer *8*, 180–192.

49. Ge, Z.S., and Liu, S.Y. (2013). Functional block copolymer assemblies responsive to tumor and intracellular microenvironments for site-specific drug delivery and enhanced imaging performance. Chem. Soc. Rev. *42*, 7289–7325.

50. Pawlak, M., Grygolowicz-Pawlak, E., and Bakker, E. (2010). Ferrocene bound poly(vinyl chloride) as ion to electron transducer in electrochemical ion sensors. Anal. Chem. *82*, 6887–6894.

51. Chang, X., Du, Z., Hu, F., Cheng, Z., Ren, B., Fu, S., and Tong, Z. (2016). Ferrocene-functionalized hydrophobically modified ethoxylated urethane: redox-responsive controlled self-assembly and rheological behavior in aqueous solution. Langmuir *32*, 12137–12145.

52. Rulkens, R., Lough, A.J., Manners, I., Lovelace, S.R., Grant, C., and Geiger, W.E. (1996). Linear oligo(ferrocenyldimethylsilanes) with between two and nine ferrocene units: electrochemical and structural models for poly(ferrocenylsilane) high polymers. J. Am. Chem. Soc. *118*, 12683–12695.

53. Tabata, Y., Murakami, Y., and Ikada, Y. (1998). Tumor accumulation of poly(vinyl alcohol) of different sizes after intravenous injection. J. Control. Release *50*, 123–133.

54. Matsumura, Y., and Maeda, H. (1986). A new concept for macromolecular therapeutics in cancer chemotherapy: mechanism of tumoritropic accumulation of proteins and the antitumor agent smancs. Cancer Res. *46*, 6387–6392.

55. Nagayasu, A., Shimooka, T., Kinouchi, Y., Uchiyama, K., Takeichi, Y., and Kiwada, H. (1994). Effects of fluidity and vesicle size on antitumor activity and myelosuppressive activity of liposomes loaded with daunorubicin. Biol. Pharm. Bull. *17*, 935–939.

56. Brillas, E., Sirés, I., and Oturan, M.A. (2009). Electro-Fenton process and related electrochemical technologies based on Fenton's reaction chemistry. Chem. Rev. *109*, 6570–6631.

57. Pignatello, J.J., Oliveros, E., and MacKay, A. (2006). Advanced oxidation processes for organic contaminant destruction based on the Fenton reaction and related chemistry. Crit. Rev. Environ. Sci. Technol. *36*, 1–84.

58. Tapeinos, C., and Pandit, A. (2016). Physical, chemical, and biological structures based on ROS-sensitive moieties that are able to respond to oxidative microenvironments. Adv. Mater. *28*, 5553–5585.

59. Hsu, P.P., and Sabatini, D.M. (2008). Cancer cell metabolism: Warburg and beyond. Cell *134*, 703–707.

60. Chang, C.H., Qiu, J., O'Sullivan, D., Buck, M.D., Noguchi, T., Curtis, J.D., Chen, Q.Y., Gindin, M., Gubin, M.M., van der Windt, G.J.W., et al. (2015). Metabolic competition in the tumor microenvironment is a driver of cancer progression. Cell *162*, 1229–1241.

61. Buiculescu, R., Stefanakis, D., Androulidaki, M., Ghanotakis, D., and Chaniotakis, N.A. (2016). Controlling carbon nanodot fluorescence for optical biosensing. Analyst *141*, 4170–4180.

62. Wilson, W.R., and Hay, M.P. (2011). Targeting hypoxia in cancer therapy. Nat. Rev. Cancer *11*, 393–410.

63. Pavlova, N.N., and Thompson, C.B. (2016). The emerging hallmarks of cancer metabolism. Cell Metab. *23*, 27–47.

64. Sim, J.W., Cowburn, A.S., Palazon, A., Madhu, B., Tyrakis, P.A., Macías, D., Bargiela, D.M., Pietsch, S., Gralla, M., Evans, C.E., et al. (2018). The factor inhibiting HIF asparaginyl hydroxylase regulates oxidative metabolism and accelerates metabolic adaptation to hypoxia. Cell Metab. *27*, 898–913.

65. Trelstad, R.L., Lawley, K.R., and Holmes, L.B. (1981). Nonenzymatic hydroxylations of proline and lysine by reduced oxygen derivatives. Nature *289*, 310–312.

66. Li, M., Xia, J., Tian, R., Wang, J., Fan, J., Du, J., Long, S., Song, X., Foley, J.W., and Peng, X. (2018). Near-infrared light-initiated molecular superoxide radical generator: rejuvenating photodynamic therapy against hypoxic tumors. J. Am. Chem. Soc. *140*, 14851–14859.

67. Xu, L., Fukumura, D., and Jain, R.K. (2002). Acidic extracellular pH induces vascular endothelial growth factor (VEGF) in human glioblastoma cells via ERK1/2 MAPK signaling pathway: mechanism of low pH-induced VEGF. J. Biol. Chem. *277*, 11368–11374.

68. Wang, B., He, X., Zhang, Z., Zhao, Y., and Feng, W. (2013). Metabolism of nanomaterials *in vivo*: blood circulation and organ clearance. Acc. Chem. Res. *46*, 761–769.

69. Feng, Q., Liu, Y., Huang, J., Chen, K., Huang, J., and Xiao, K. (2018). Uptake, distribution, clearance, and toxicity of iron oxide nanoparticles with different sizes and coatings. Sci. Rep. *8*, 2082–2094.

70. Warburg, O. (1956). On the origin of cancer cells. Science *123*, 309–314.

71. Patra, M., Awuah, S.G., and Lippard, S.J. (2016). Chemical approach to positional isomers of glucose-platinum conjugates reveals specific cancer targeting through glucose-transporter-mediated uptake *in vitro* and *in vivo*. J. Am. Chem. Soc. *138*, 12541–12551.

72. Szatrowski, T.P., and Nathan, C.F. (1991). Production of large amounts of hydrogen peroxide by human tumor cells. Cancer Res. *51*, 794–798.

73. Noh, J., Kwon, B., Han, E., Park, M., Yang, W., Cho, W., Yoo, W., Khang, G., and Lee, D. (2015). Amplification of oxidative stress by a dual stimuli-responsive hybrid drug enhances cancer cell death. Nat. Commun. *6*, 6907–6925.